Light-induced anomalous Hall effect in graphene

J.W. McIver[1*], B. Schulte[1*], F.-U. Stein[1*], T. Matsuyama[1], G. Jotzu[1], G. Meier[1] and A. Cavalleri[1,2]

Many striking non-equilibrium phenomena have been discovered or predicted in optically-driven quantum solids[1], ranging from light-induced superconductivity[2,3] to Floquet-engineered topological phases[4-8]. These effects are expected to lead to dramatic changes in electrical transport, but can only be comprehensively characterized or functionalized with a direct interface to electrical devices that operate at ultrafast speeds[1-8]. Here, we make use of laser-triggered photoconductive switches[9] to measure the ultrafast transport properties of monolayer graphene, driven by a mid-infrared femtosecond pulse of circularly polarized light. The immediate goal of this experiment is to probe the transport signatures of a predicted photon-dressed topological band structure in graphene[4,5], similar to the one originally proposed by Haldane[10]. We report the observation of an anomalous Hall effect in the absence of an applied magnetic field. The dependence of the effect on a gate potential used to tune the Fermi level reveals multiple features that directly reflect the dressed band structure expected from Floquet theory, including a ~60 meV wide plateau centered at the Dirac point. We find that when the Fermi level lies within this plateau, the anomalous Hall conductance approaches $2e^2/h$.

Optical driving has been proposed as a means to engineer topological properties in topologically trivial systems[4-8]. One proposal for such a 'Floquet topological insulator' is based on breaking time-reversal symmetry in graphene through a coherent interaction with circularly polarized light[4]. In this theory, the light field drives electrons in circular trajectories through the band structure. Close to the Dirac point, these states are predicted to acquire a non-adiabatic Berry phase every optical cycle, which is equal and opposite for the upper and lower band. This time-averaged extra phase accumulation amounts to an energy shift that would lift the degeneracy of the Dirac point, opening a topological gap in the emergent photon-dressed band structure (Fig. 1).

* These authors contributed equally to this work
[1] Max Planck Institute for the Structure and Dynamics of Matter, Hamburg, Germany
[2] Department of Physics, Clarendon Laboratory, University of Oxford, Oxford, UK
email: andrea.cavalleri@mpsd.mpg.de; james.mciver@mpsd.mpg.de

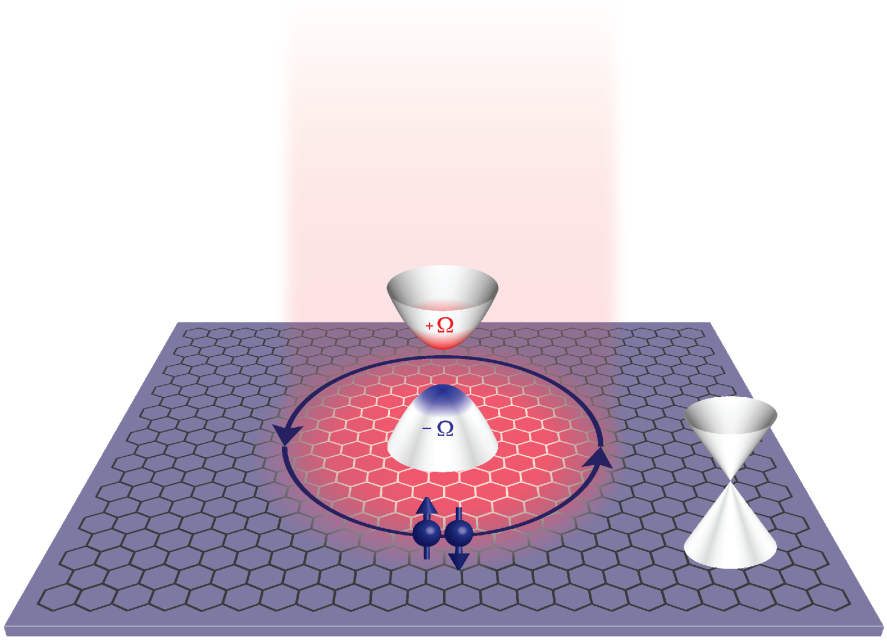

Fig. 1 | **Photon-dressed topological band structure in graphene.** A coherent interaction with circularly polarized light is predicted to open a topological band gap in the graphene dispersion[4]. The gap is characterized by the presence of Berry curvature (Ω), which is identical in both valleys. The experimental signature of the induced nontrivial topology is the emergence of anomalous Hall currents.

The non-trivial topology of the dressed bands forming this gap arises from their nonzero Berry curvature distribution[4,5], which integrated over the Brillouin zone defines a topological invariant, called the Chern number[11-14]. Topologically protected transport is predicted to develop if the Fermi level (E_F) lies inside the gap, exhibiting a quantized anomalous Hall conductance of $2e^2/h$ in the absence of an applied magnetic field[5,10-15]. This corresponds to the formation of a light-induced Chern insulator, equivalent to the phase originally proposed by Haldane[10] and distinct from topological phases induced by spin-orbit interaction[12-14,16,17].

Whilst quantum simulation experiments have validated aspects of this proposal in synthetic physical settings[18,19], and Floquet-Bloch states have been detected in a topological insulator[20], light-induced anomalous Hall currents and the accompanying dressed topological band structure have not been observed in a real material.

Inducing and detecting anomalous Hall currents in graphene presents multiple experimental challenges. The laser electric field strength required to open an observable topological gap is estimated to be ~ 10^7-10^8 V/m, even at mid-infrared wavelengths where the effect is enhanced[4,5,15]. Hence, to avoid material damage whilst still providing sufficient field strength, ultrafast laser pulses must be used. Consequently, the resulting Hall conductance changes are too short-lived to be probed with conventional transport techniques.

In this work, ultrafast anomalous Hall currents were detected on-chip by using a laser-triggered photoconductive switch[9,21-23].

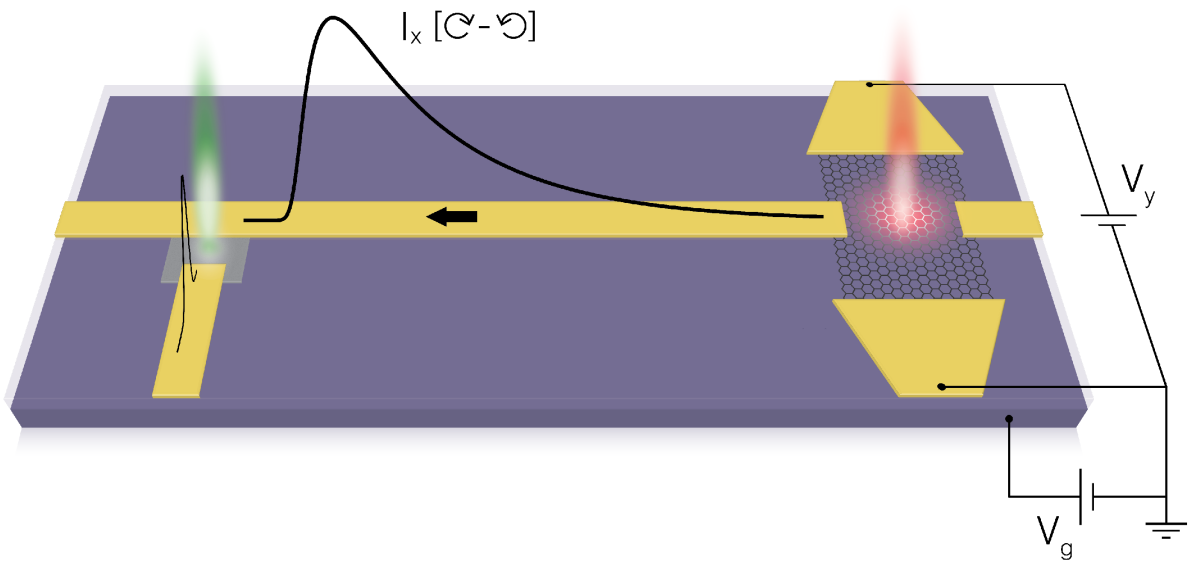

Fig. 2 | **Device architecture used to detect ultrafast anomalous Hall currents in graphene.** Exfoliated graphene monolayer with four electrical contacts (right) and a photoconductive switch for current detection (left), connected by a microstrip transmission line. The graphene was optically driven using an ultrafast mid-infrared circularly polarized laser pulse (red beam). The generated helicity-dependent anomalous Hall currents I_x [↻ - ↺] were probed after a variable time delay at the photoconductive switch, which was activated by a second laser pulse (green beam). Anomalous Hall currents were measured as a function of source-drain voltage bias V_y and backgate voltage V_g, the latter of which controlled the graphene Fermi level (E_F).

A schematic of our device architecture is shown in Fig. 2. An exfoliated monolayer graphene flake ($\sim$ 30 x 20 μm^2) was transferred onto a doped silicon wafer with an oxide layer and contacted in a four-probe Hall geometry using standard lithography procedures[24,25]. The metallic leads formed microstrip transmission lines in conjunction with the oxide layer and silicon wafer. These routed ultrafast anomalous Hall currents generated in the graphene to a photoconductive switch for detection. The switch consisted of a resistive amorphous silicon patch that bridged the main transmission line and a probing line. When excited with a visible ultrafast laser pulse, the switch became highly conductive and detected currents flowing in the main transmission line with a time resolution set by the silicon carrier lifetime ($\sim$ 1 ps). By adjusting the time delay between the graphene laser drive pulse (pump) and the switch trigger pulse (probe), the temporal profile of ultrafast anomalous Hall currents could be characterized.

Graphene was driven using a $\sim$ 500 fs laser pulse at a frequency of $\sim$ 46 THz (photon energy $\hbar\omega \sim$ 191 meV, wavelength $\sim$ 6.5 μm). Unless otherwise noted, a peak laser pulse fluence of $\sim$ 0.23 mJ/cm^2 was used, corresponding to a peak intensity of $\sim$ 4.3 x 10^{12} W/m^2 and peak electric field strength of $\sim$ 4.0 x 10^7 V/m (in free space, for circular polarization). The pulses were focused to a spot size of $\sim$ 80 μm (FWHM), ensuring homogeneous illumination of the graphene flake and the contacts. A second ultrafast laser pulse centered at 520 nm was used to operate the photoconductive switch. The device was mounted in a microscopy cryostat designed for high-frequency transport measurements and cooled to a base temperature of 80 K. A global backgate formed by the silicon wafer and the oxide layer controlled the Fermi level (E_F) in the graphene flake. The graphene field-effect mobility was measured to be $\mu \sim$ 10,000 cm^2/Vs in the vicinity of the Dirac point. The results presented here are from a single device, and consistent results have been obtained using five different devices.

Anomalous Hall currents induced by circularly polarized light are expected to exhibit the following traits: (1) They should be generated in the transverse direction (I_x) with respect to an applied DC voltage bias (V_y). (2) They should reverse polarity upon reversing the light helicity. (3) They should reverse polarity upon reversing V_y, with a linear functional dependence. To probe (1) and (2), we directly detected the difference between currents I_x

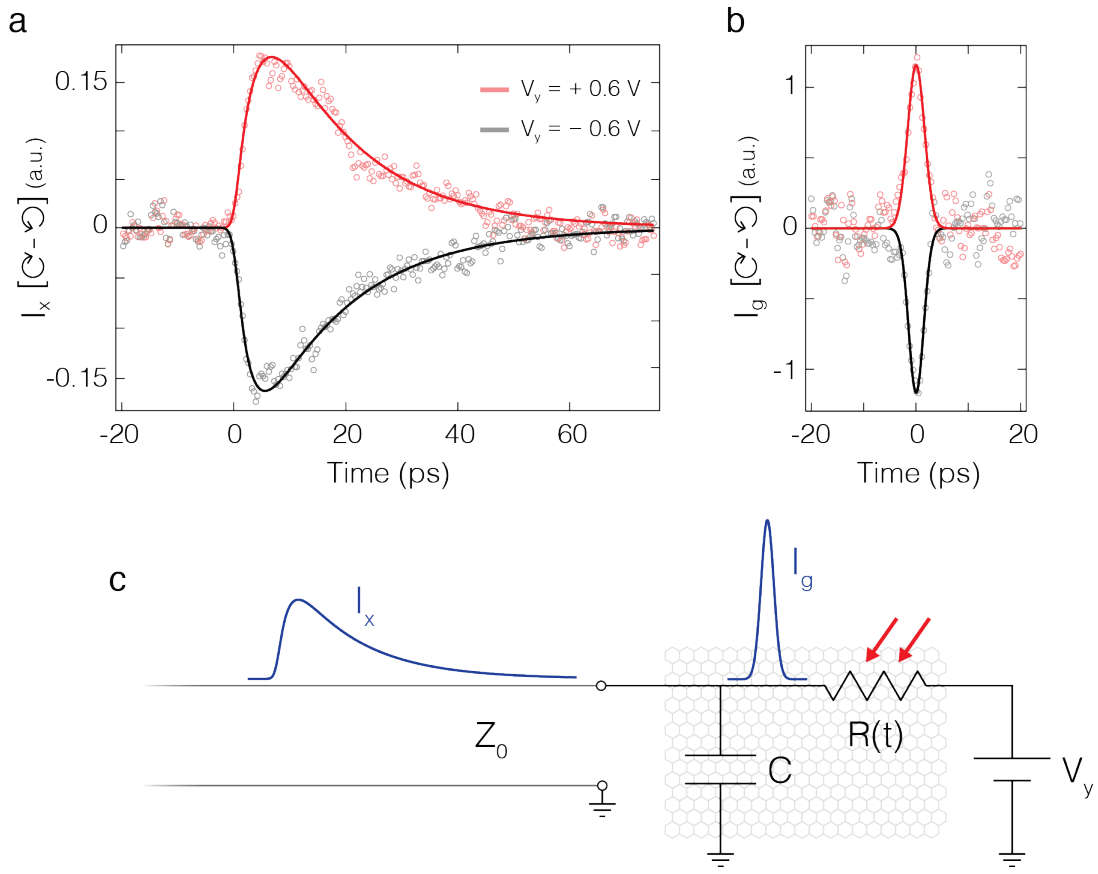

Fig. 3 | **Ultrafast anomalous Hall currents in graphene driven by circularly polarized light.** **a**, Time-resolved helicity-dependent anomalous Hall currents I_x [↻ - ↺] measured at the photoconductive switch for a positive (red) and negative (black) transverse source-drain voltage V_y. The graphene Fermi level was gated to the Dirac point ($E_F = 0$). Solid lines are fits using the circuit model sketched in c. A small background observed at $V_y = 0$ was subtracted from the data sets (see supplementary information). **b**, Reconstructed anomalous Hall current signals I_g accounting for the effect of the graphene capacitance and transmission line dispersion. **c**, Simplified effective circuit diagram relating the measured signals I_x and the reconstructed signals I_g. R and C are the graphene resistance and capacitance, and Z_0 is the impedance of the microstrip transmission line.

generated with right- versus left-circular polarization (henceforth referred to as I_x [↻ - ↺]), utilizing an optical polarization chopping technique.

Figure 3a displays the measured I_x [↻ - ↺] signal as a function of pump-probe time delay for a positive and negative V_y, with the Fermi level gated to the equilibrium graphene Dirac point ($E_F = 0$). The time-resolved signal exhibits a fast rise time followed by an exponential decay, and reverses polarity upon reversing V_y.

Note that the data in Fig. 3a do not directly reflect the timescale that anomalous Hall currents persist in the graphene. Due to the capacitive coupling between the graphene and the underlying substrate, a low-pass filter was formed in conjunction with the transmission line impedance Z_0 (Fig. 3c). This had the effect of integrating ultrafast currents generated in the graphene before discharging them into the transmission line. By fitting the exponential decay of the signals in Fig. 3a, the effective RC time constant for the discharge process could be determined, which we also verified using circuit simulations. This information allowed us to retrieve the original current profiles using the transfer function for a low-pass filter (see supplementary information). Figure 3b shows the reconstructed current signals, also accounting for transmission line dispersion, which establish an upper bound of $\sim$ 3 ps for the time that anomalous Hall currents persist in the graphene.

Having established the presence of ultrafast anomalous Hall currents in graphene, we investigated the functional dependence of I_x [↻ - ↺] on V_y at $E_F = 0$. We did so by fixing the pump-probe time delay at the maximum of the I_x [↻ - ↺] signal in Fig. 3a, which we henceforth refer to as $\hat{I}_x$ [↻ - ↺], and measured the signal amplitude as a function of V_y (Fig. 4a). The data exhibit the expected linear dependence (requirement 3).

We also investigated helicity-dependent currents generated in response to a longitudinal voltage bias V_x (Fig. 4b), which should be forbidden by symmetry. The data in Fig. 4b confirm that no helicity-dependent longitudinal currents were generated.

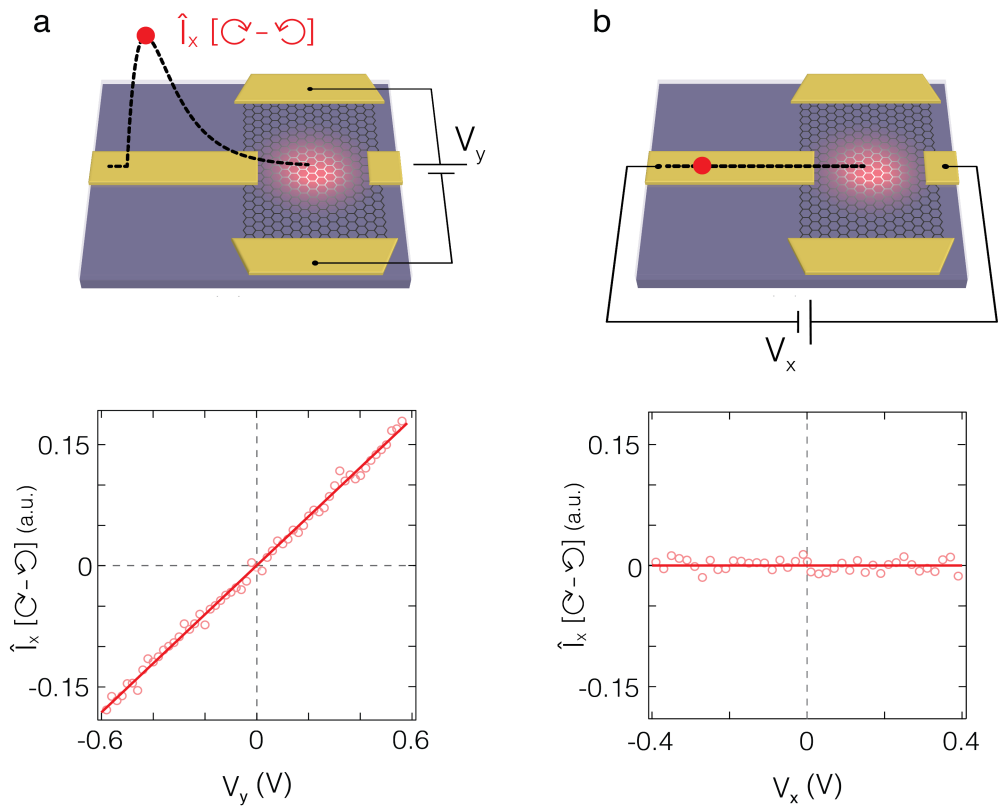

Fig. 4 | Helicity-dependent current behavior under different source-drain voltage geometries. The peak of the helicity-dependent current $\hat{I}_x$ [↻ - ↺] measured as a function of **a**, transverse source-drain voltage V_y and **b**, longitudinal source-drain voltage V_x. The graphene Fermi level was gated to the Dirac point ($E_F = 0$). Solids lines are linear fits.

By characterizing the responsivity of the photoconductive switch and simulating the impedance of our transmission line at THz frequencies, we estimated the peak non-equilibrium anomalous Hall conductance, which we define as $G_{xy} = \hat{I}_g$ [↻ - ↺] / $2V_y$, where $\hat{I}_g$ is the peak of the reconstructed signal in Fig. 3b.

Figure 5a displays G_{xy} as a function of the laser drive pulse fluence, measured for $E_F = 0$. In these measurements, G_{xy} grew linearly from zero at low laser fluences and saturated at higher fluences. At the highest fluence, we extracted a value $G_{xy} \cong (1.8 \pm 0.4)\ e^2/h$ (see supplementary information). According to models for optically-driven graphene, $G_{xy} \approx 2e^2/h$ is predicted to result from the emergence of a photon-dressed topological band structure, provided that E_F lies inside the gap that opens at the Dirac point[5,15,26-28].

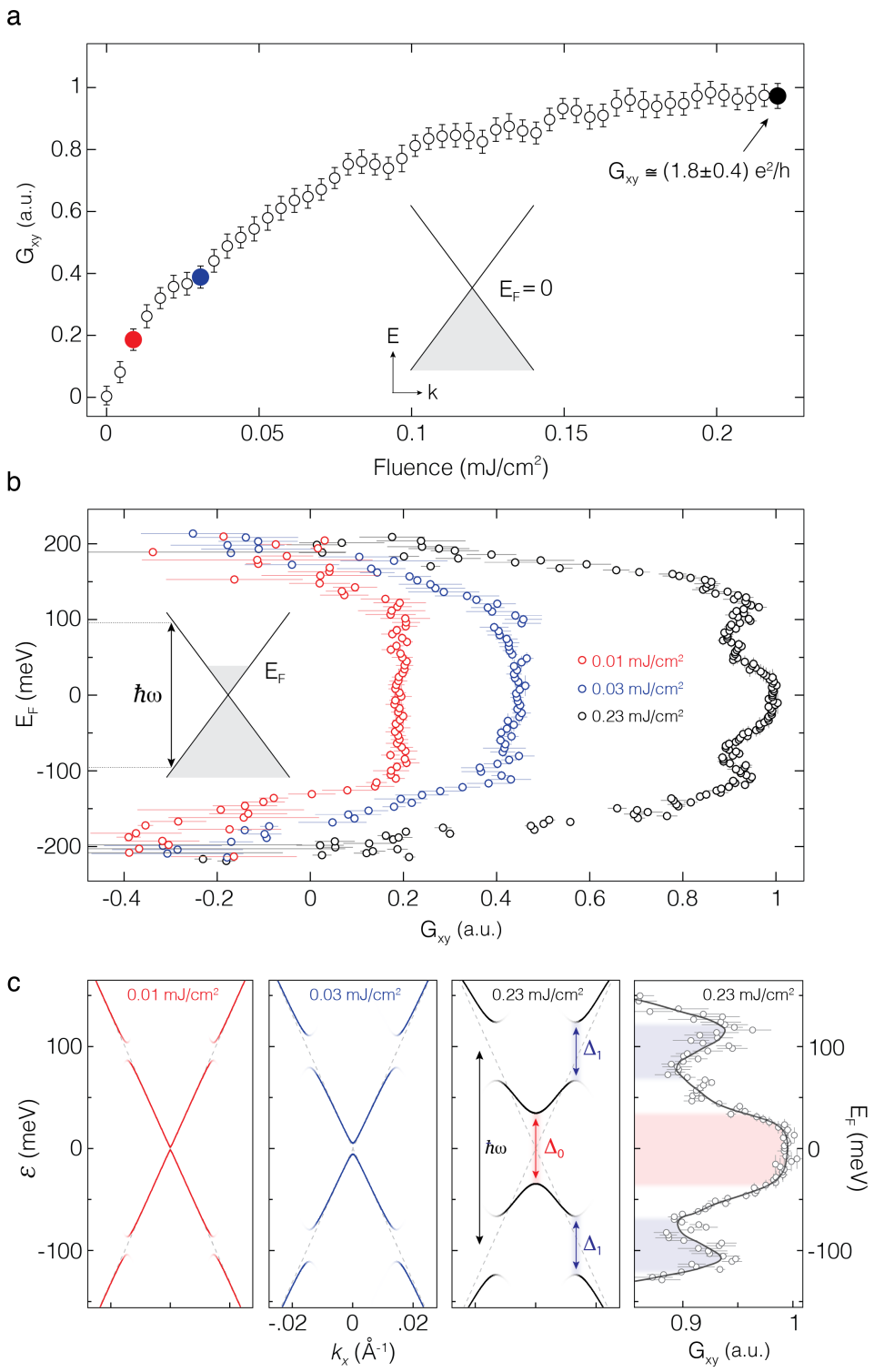

Fig. 5 | Evidence for a photon-dressed topological band structure. a, Non-equilibrium anomalous Hall conductance G_{xy} as a function of the peak laser drive pulse fluence. The equilibrium Fermi level was gated to the Dirac point ($E_F = 0$). Error bars are the standard error. Colored data points correspond to the fluences measured in b. **b**, G_{xy} as a function of E_F measured at three fluences. Horizontal error bars are the standard error and vertical error bars denote the uncertainty related to determining the precise value of the Dirac point. **c**, Left three panels: Dressed band structures for the fluences reported in b simulated using Floquet theory. At the highest fluence, we calculated $\Delta_0 \cong 69$ meV and $\Delta_1 \cong 56$ meV. Right panel: Blow up of the high-fluence data in b for comparison. Solid line is the smoothed data. Shaded regions highlight the features corresponding to light-induced band gaps in the Floquet band structure.

To characterize the predicted dressed topological bands, we varied the equilibrium E_F using the backgate[29] and compared the variation in G_{xy} (Fig. 5b) with calculations of the expected dressed band structures based on Floquet theory, using our laser pulse parameters (Fig. 5c) (see supplementary information).

For low drive fluence (red circles), G_{xy} was observed to be independent of the backgate potential for $|E_F| \lesssim \hbar\omega/2$, where direct interband transitions are allowed. This suggests that as the predicted gaps Δ_1 open at $\pm\hbar\omega/2$ in the dressed band structure, the resulting electron distribution acts as a source of anomalous Hall currents. For $|E_F| \gtrsim \hbar\omega/2$, G_{xy} decreased to zero and changed sign when approaching the dielectric breakdown threshold of the device.

The gaps Δ_1 result from resonant Rabi splitting and are predicted to affect the Berry curvature distribution in the dressed bands[4,15,26-28,30], which will in turn affect the G_{xy} spectrum. Indeed, as the fluence was increased (blue and black circles), features emerged near $\pm\hbar\omega/2$ that are closely aligned with the gaps Δ_1.

At the highest fluence (black circles), close to the Dirac point and away from the resonance, a conductance plateau was observed for $|E_F| \lesssim 30$ meV, where $G_{xy} \cong (1.8 \pm 0.4)\ e^2/h$. Remarkably, the width of the plateau is very close to the calculated width of the light-induced topological gap at the Dirac point Δ_0 (69 meV, red shading). For $|E_F| \gtrsim \Delta_0/2$, G_{xy} decreased, as predicted due to the reduced net Berry curvature of the occupied dressed electronic states[11-14]. The sharpness of this decrease may depend on multiple factors, including the Berry curvature and non-equilibrium electron distributions in the dressed bands, which is influenced by the frequency, amplitude and pulse-shape of the laser, as well as disorder, interactions and dissipation[4,15,26-28,30].

In summary, utilizing ultrafast transport techniques we observed a light-induced anomalous Hall effect in graphene that displayed multiple signatures of an emergent photon-dressed topological band structure. Most strikingly, despite the non-equilibrium nature of our measurements, the extracted value of the anomalous Hall conductance in a plateau encompassing the Dirac point lies in the same quantitative range as that expected for an equilibrium Chern insulator with a Chern number of one[10].

Experimental advances utilizing encapsulated graphene heterostructures will open up the regime $|E_F| >> \hbar\omega/2$, where G_{xy} reverses sign, in future experiments. The on-chip ultrafast transport techniques presented here will also enable inroads into other compelling problems in quantum materials, including the non-equilibrium control of van der Waals heterostructures such as twisted bilayer graphene[31], transition metal dichalcogenides[32], materials undergoing photo-induced phase transitions[33], and the physics of non-equilibrium superconductors[2-3].

References

1. Basov, D. N., Averitt, R. D. & Hsieh, D. Towards properties on demand in quantum materials. *Nat. Mat.* **16**, 1077-1088 (2017).
2. Fausti, D. et al. Light-induced superconductivity in a stripe-ordered cuprate. *Science* **331**, 189-191 (2011).
3. Mitrano, M. et al. Possible light-induced superconductivity in K_3C_{60} at high temperature. *Nature* **530**, 461-464 (2016).
4. Oka, T. & Aoki, H. Photovoltaic Hall effect in graphene. *Phys. Rev. B* **79**, 081406(R) (2009).
5. Kitagawa, T., Oka, T., Brataas, A., Fu, L. & Demler, E. Transport properties of nonequilibrium systems under the application of light: Photoinduced quantum Hall insulators without Landau levels. *Phys. Rev. B* **84**, 235108 (2011).
6. Lindner, N. H., Refael, G. & Galitski, V. Floquet topological insulator in semiconductor quantum wells. *Nat. Phys.* **7**, 490-495 (2011).
7. Sie, E. et al. Valley-selective optical Stark effect in monolayer WS_2. *Nat. Mat.* **14**, 290-294 (2015).
8. Bukov, M., D'Alessio, L. & Polkovnikov, A. Universal high-frequency behavior of periodically driven systems: from dynamical stabilization to Floquet engineering. *Adv. In Phys.* **64**, 2 139-226 (2015).
8. Auston, D. H. Picosecond optoelectronic switching and gating in silicon. *Appl. Phys. Lett.* **26**, 3 (1975).
10. Haldane, F. D. M. Model for a Quantum Hall Effect without Landau Levels: Condensed-Matter Realization of the "Parity Anomaly". *Phys. Rev. Lett.* **61**, 2015-2018 (1988).
11. Xiao, D., Chang, M.-C. & Niu, Q. Berry phase effects on electronic properties. *Rev. Mod. Phys.* **82**, 1959 (2010).
12. Hasan, M. Z. & Kane, C. L. Colloquium: Topological insulators. *Rev. Mod. Phys.* **82**, 3045-3067 (2010).
13. Qi, X.-L. & Zhang, S.-C. Topological insulators and superconductors. *Rev. Mod. Phys.* **83**, 1057 (2011).
14. Bernevig, B. A. & Hughes, T.L., *Topological insulators and topological superconductors. Princeton University Press, Princeton, New Jersey* (2013).
15. Foa Torres, L. E. F., Perez-Piskunow, P. M., Balseiro, C. A. & Usaj, G. Multiterminal Conductance of a Floquet Topological Insulator. *Phys. Rev. Lett.* **113**, 266801 (2014).
16. Chang, C.-Z. et al. Experimental Observation of the Quantum Anomalous Hall Effect in a Magnetic Topological Insulator. *Science* **340**, 176-170 (2013).
17. König, M. et al. Quantum Spin Hall Insulator State in HgTe Quantum Wells. *Science* **318**, 766-770 (2007).
18. Rechtsman, M. C. et al. Photonic Floquet topological insulator. *Nature* **496**, 196-200 (2013).

19. Jotzu, G. et al. Experimental realization of the topological Haldane model with ultracold fermions. *Nature* **515**, 237-240 (2014).
20. Wang, Y. H., Steinberg, H., Jarillo-Herrero, P. & Gedik, N. Observation of Floquet-Bloch States on the Surface of a Topological Insulator. *Science* **342**, 453-457 (2013).
21. Zhong, Z., Gabor, N. M., Sharping , J. E., Gaeta, A. L. & McEuen, P. L. Terahertz time-domain measurement of ballistic electron resonance in a single-walled carbon nanotube. *Nat. Nano.* **3**, 201-205 (2008).
22. Prechtel, L. et al. Time-resolved ultrafast photocurrents and terahertz generation in freely suspended graphene. *Nat. Comm.* **3**, 646 (2012).
23. Hunter, N. et al. On-Chip Picosecond Pulse Detection and Generation Using Graphene Photoconductive Switches. *Nano Lett.* **15**, 1591-1596 (2015).
24. Geim, A. K. & Novoselov, K. S. The rise of graphene. *Nat. Mat.* **6**, 183-191 (2007).
25. Zhang, Y., Tan, Y.-W., Stormer, H. L. & Kim, P. Experimental observation of the quantum Hall effect and Berry's phase in graphene. *Nature* **438**, 201-204 (2005).
26. Usaj, G., Perez-Piskunow, P. M., Foa Torres, L. E. F. & Balseiro, C. A. Irradiated graphene as a tunable Floquet topological insulator. *Phys. Rev. B* **90**, 115423 (2014).
27. Mikami, T. et al. Brillouin-Wigner theory for high-frequency expansion in periodically driven systems: Application to Floquet topological insulators. *Phys. Rev. B* **93**, 144307 (2016).
28. Dehghani, H., Oka, T., Mitra, A. Out-of-equilibrium electrons and the Hall conductance of a Floquet topological insulator. *Phys. Rev. B* **91**, 155422 (2015).
29. Wang, F. et al. Gate-Variable Optical Transitions in Graphene. *Science* **320**, 206-209 (2008).
30. Sentef, M. A. et al. Theory of Floquet band formation and local pseudospin textures in pump-probe photoemission of graphene. *Nat. Comm.* **6**, 7047 (2015).
31. Cao, Y. et al. Unconventional superconductivity in magic-angle graphene superlattices. *Nature* **556**, 43-50 (2018).
32. Xu, X., Yao, W., Xiao, D. & Heinz, T. F. Spin and pseudospins in layered transition metal dichalcogenides. *Nat. Phys.* **10**, 343-350 (2014).
33. Stojchevska, L. et al., Ultrafast Switching to a Stable Hidden Quantum State in an Electronic Crystal. *Science* **344**, 177-180 (2014).

Supplementary information for

Light-induced anomalous Hall effect in graphene

J.W. McIver*, B. Schulte*, F.-U. Stein*, T. Matsuyama, G. Jotzu, G. Meier and A. Cavalleri

Table of contents

S1. Experimental setup and methods

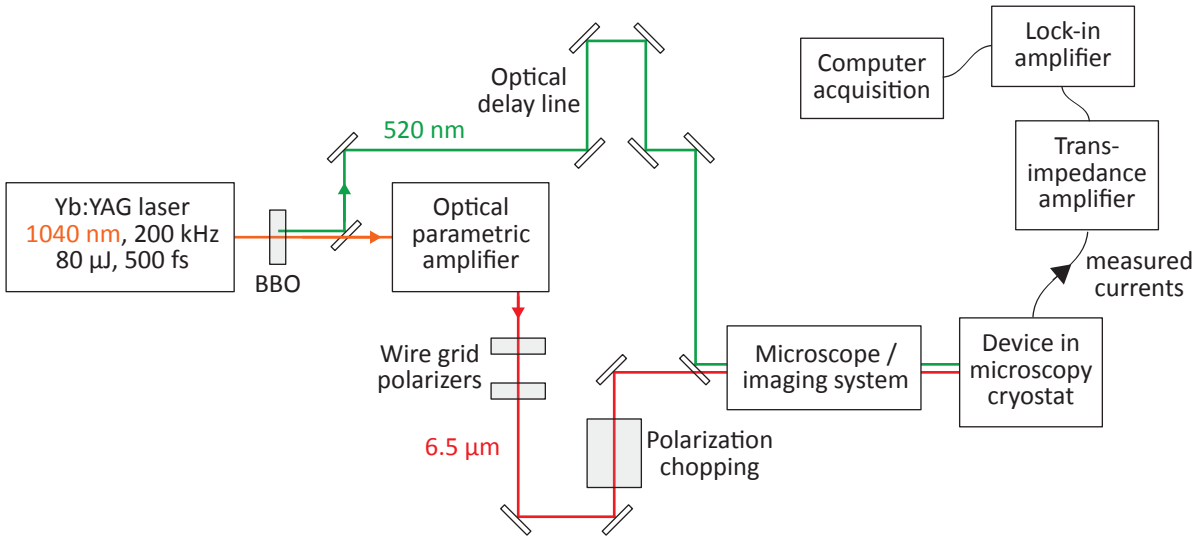

Fig. S1 | Block diagram of the experimental setup.

Setup overview. A block diagram of the experimental setup used to induce and probe ultrafast anomalous Hall currents in graphene is depicted in Fig. S1. A train of ultrafast laser pulses with a central wavelength of 1040 nm, pulse duration of ~ 500 fs and pulse energy of ~ 80 µJ were derived from a commercial Yb-based laser system. It operated at 200 kHz with an average power of 16 W. Approximately 1% of the total power was converted to the second harmonic wavelength of 520 nm by passing the beam through a Beta Barium Borate (BBO) crystal. The remaining 1040 nm light was separated from the 520 nm light using a dichroic mirror and fed into a home-built optical parametric amplifier[34] with a difference frequency generation stage. This produced mid-infrared laser pulses at 6.5 µm with a pulse duration of ~ 500 fs.

The mid-infrared beam was passed through two wire-grid polarizers, which were used to adjust the intensity and linear polarization of the light. A quarter-waveplate mounted in a hollow-bore motor was used to perform helicity-dependent measurements using a polarization chopping technique (discussed below). From there the beam was coupled into a microscope and focused onto the graphene device at normal incidence with a ~ 80 µm focused spot size (FWHM) so that the graphene and contacts were homogeneously

illuminated. The device was mounted in a microscopy cryostat designed for high frequency transport measurements and cooled to a base temperature of 80 K for all measurements.
The 520 nm laser beam generated at the output of the laser was routed through an optical delay line, coupled into the microscope and used to operate the photoconductive switch using a peak fluence of ~ 15 mJ/cm^2. A microscope camera provided a live video feed of the laser beam and device alignment, which was maintained using active stabilization techniques. By adjusting the path length of the optical delay line, the timing between the 6.5 μm graphene optical drive pulse (pump) and the 520 nm switch trigger pulse (probe) could be varied and ultrafast anomalous Hall currents detected with a ~ 1 ps time resolution. Detected currents were amplified using a home-built transimpedance amplifier and processed using standard lock-in techniques.

Optical polarization chopping. We isolated helicity-dependent currents using optical polarization chopping[35]. A hollow-bore motor was used to continuously rotate a quarter-waveplate at a frequency of ~ 400 Hz. The mid-infrared polarization then changed helicity four times per 360-degree revolution. By triggering on the 2nd harmonic of the rotation frequency, helicity-dependent signals could be isolated using a lock-in amplifier. We calibrated the phase of the lock-in amplifier by performing optical polarization measurements at the sample position.

Intensity dependence data. The data in Figure 5a (main text) is the average of $\hat{I}_x[\circlearrowright - \circlearrowleft] / 2V_y$ measured with V_y = +0.6 V and V_y = -0.6 V at E_F = 0 meV, which is directly proportional to G_{xy} (see section S3.3).

Backgate dependence data. The data in Figure 5b (main text) is the average of $\hat{I}_x[\circlearrowright - \circlearrowleft] / 2V_y$ measured with a positive and negative V_y, which is directly proportional to G_{xy} (see section S3.3). Measurements were performed by applying +/- 12.5 V over a 100 kΩ resistor in series with the source so that the source-drain current running through the graphene was held approximately constant at ~ 125 μA for all gate voltages. This was done to prevent large source-drain currents from breaking the contacts as the graphene carrier density was increased by the gate. While measuring $\hat{I}_x[\circlearrowright - \circlearrowleft]$ at different backgate voltages, the current outputted by the source was simultaneously recorded and the DC source-drain voltage drop V_y could be determined and used to calculate $\hat{I}_x[\circlearrowright - \circlearrowleft] / 2V_y$.

The equilibrium Fermi level position was calculated using the relation $E_F = \mathrm{sign}(n)\ \hbar\ v_f \sqrt{\pi\ |n|}$, after ref.[29], where v_f is the Fermi velocity (we use v_f = 1 x 10^6 ms^{-1}), n = C (V - V_D) / e is the graphene carrier density, C = $\varepsilon_0\varepsilon_r$ / d is the capacitance per area of the graphene/SiO_2 stack, e is the electron charge, V_D is the Dirac point, V is the applied gate voltage, the thickness d = 285 nm and ε_r = 3.9. The transfer characteristic is shown in Fig. S2e.

S2. Device fabrication and characterization

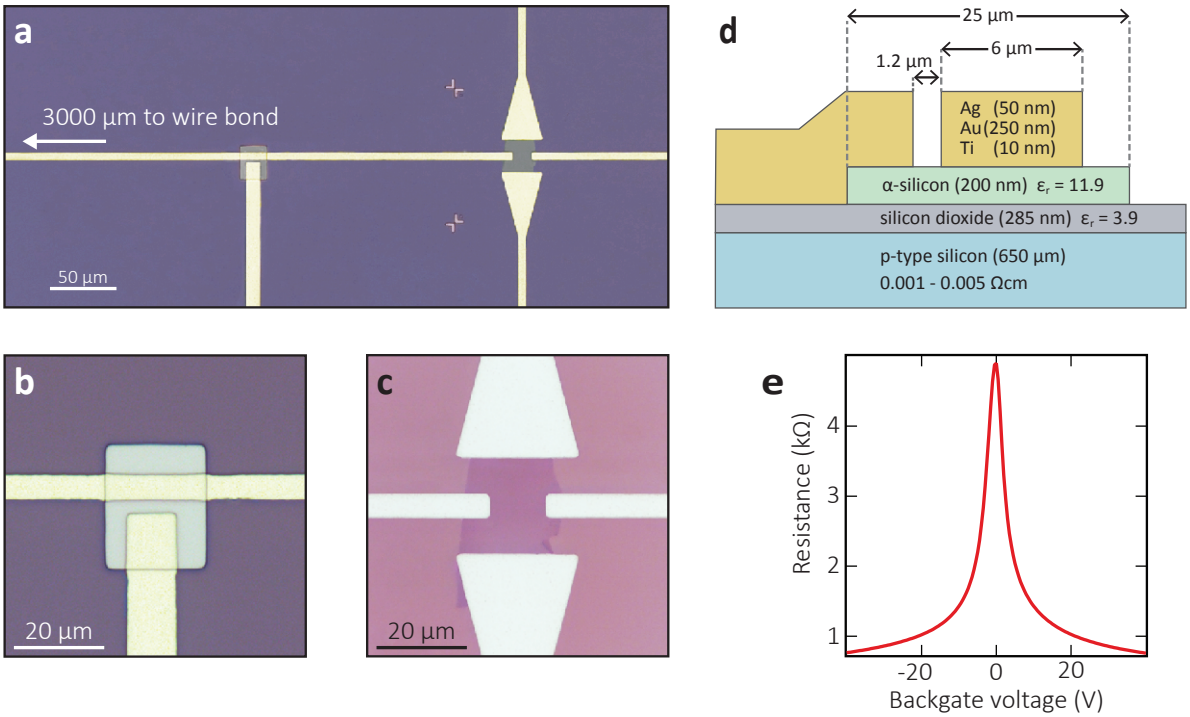

Fig. S2 | **Sample geometry and transport characteristics. a**, Optical microscopy image of the device studied in the main text. **b**, Close-up of the silicon photoconductive switch. **c**, Close-up of the contacted graphene flake. **d**, Schematic cross-section at the photoconductive switch position (not to scale). **e**, Graphene transfer characteristic: two-point resistance measurement between the large graphene contacts as a function of backgate voltage. The graphene charge neutrality point remained at a backgate voltage between -1 V and +1 V for all measurements reported in the paper.

Single layer graphene was obtained by mechanical exfoliation. Subsequently, the ultrafast optoelectronic circuitry was fabricated using standard laser lithography, thermal evaporation, and lift-off processing techniques.

Figure S2a-c shows microscope images of the graphene device studied in the main text. Graphene was mechanically exfoliated from Kish graphite by the tape method[24,25] and transferred onto a highly doped p-type silicon wafer with a 285 nm SiO_2 layer. The investigated single layer graphene flake was identified by optical contrast imaging and Raman spectroscopy. After choosing the flake, the optoelectronic circuitry was fabricated in two steps. First, an amorphous silicon (α-silicon) patch was thermally evaporated in close proximity to the graphene flake. This formed the base of the photoconductive switch (Fig. S2b). Second, layered Ti/Au/Ag metallic structures were deposited to create signal lines.

These formed microstrip transmission lines in conjunction with the doped silicon wafer that were capable of transporting ultrafast currents. Four such signal lines were contacted to the graphene flake (Fig. 2c). One of these lines also passed over the α-silicon patch. The α-silicon patch was contacted with an additional sampling line so that a narrow semiconducting channel was formed between the main signal line and the sampling line (Fig. S2b). Together this structure formed the photoconductive switch. A schematic cross-section at the photoconductive switch position is shown in Fig. S2d. The circuitry is discussed in detail in the next section.

For both steps a bilayer photoresist system was used. The bottom layer was a heat-resistant undercut layer of *MicroChem LOR-7B*. The second layer consisted of positive photoresist *micro resist map-1205*. The structures were written with a direct-write laser lithography system. Afterwards the structures were developed and material was evaporated via thermal evaporation. The prepared chip was glued onto a printed circuit board chip carrier and contacted with wire bonds. To perform DC transport and optoelectronic measurements, the chip carrier was loaded into an optical microscopy cryostat equipped with low capacitance cables that connected the device to measurement electronics outside the cryostat.

The silicon substrate with oxide layer was used as a global backgate to control the graphene Fermi level. A two-point resistance measurement as a function of backgate voltage is shown in Fig. S2e. After spending time in vacuum and laser annealing with 6.5 µm light, the charge neutrality point settled very close to 0 V backgate voltage and remained between +1 V and -1 V for all measurements reported in the paper. The field-effect carrier mobility was determined to be $\mu \sim 10{,}000\ cm^2/Vs$ at a temperature of ~ 80K.

S3. Ultrafast circuitry

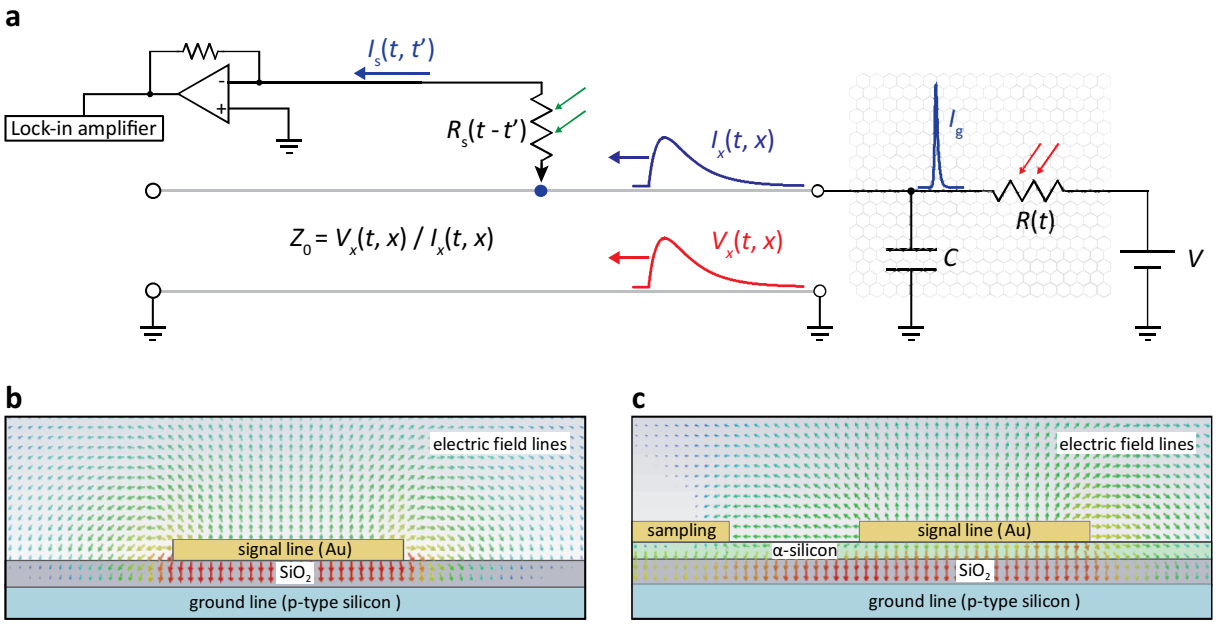

Fig. S3 | Equivalent circuit model of ultrafast current generation, propagation and detection. **a**, A current pulse I_g is generated in the graphene, which is sourced from a voltage biased light-controlled resistor *R(t)*. The graphene capacitance, *C*, has the effect of integrating the generated current before discharging it into the microstrip transmission line with a time constant $\tau_{RC} \approx Z_0 C$, where Z_0 is the transmission line impedance. I_x is the discharged current. At the position x_s the photoconductive switch (excited at time t') is modeled by a light-controlled resistor $R_s(t - t')$ that probes the local voltage profile V_x of the current pulse in the transmission line. **b**, Simulation of the electric field line distribution in the transmission line at a fixed point in space and time (cross-sectional view). **c**, Electric field line simulation at the switch position. The field lines bend in the direction of the sampling line and create a current when the switch is illuminated by laser light.

S3.1: Equivalent circuit model

Current generation. An equivalent circuit model of the optoelectronic device architecture used to generate and detect ultrafast anomalous Hall currents in graphene is shown in Fig. S3a. The source of the current generation can be modeled as a light-controlled adjustable resistor $R(t)$, representing the graphene anomalous Hall resistance, in series with a voltage source V. Before the light pulse arrives, the anomalous Hall conductance is zero corresponding to $R = \infty$ (open circuit). When the light is on, the anomalous Hall conductance becomes finite and a current I_g flows through the resistor due to the applied voltage bias. The light-induced resistance can be expected to be large compared to the load, which is

dominated by the microstrip transmission line impedance ($Z_0 \sim 8.5\pm1.0\ \Omega$). This guarantees that the majority of the photocurrent is discharged from the graphene. In other words, the graphene acts as an efficient current source.

The capacitive coupling between the graphene flake and the underlying doped Si substrate is non-negligible and can be modeled as a capacitor C in series to ground with the source resistance R. The capacitor forms a low-pass filter in conjunction with the transmission line impedance Z_0 that has the effect of integrating the pulsed photocurrent I_g before discharging it into the transmission line. The integrated temporal profile of I_g is thus encoded in the rising edge of the current pulse I_x that is injected into the transmission line. As the laser pulse subsides, $R \rightarrow \infty$ and $I_g \rightarrow 0$, and the capacitor discharges with a characteristic time constant $\tau_{RC} \sim Z_0 C$, which corresponds to the exponential decay of I_x.

Signal propagation. The pulsed signal that is injected into the transmission line is characterized by a transient current component $I_x(t, x)$ and a voltage component $V_x(t, x)$ that vary in time and space. They are self-propagated by local AC electric and magnetic fields that are near-field confined to the transmission line. The fields form a quasi-TEM mode that moves with a group velocity $v = c / \sqrt{\varepsilon_{eff}} \sim c/2$ in the present experiment, where $\varepsilon_{eff} \sim 4$ is the effective dielectric constant of the transmission line geometry and c is the speed of light. Since there are no travelling waves in any other directions, $V_x(t, x)$ and $I_x(t, x)$ are inevitably coupled at any position along the line by the characteristic impedance of the transmission line $Z_0 = V_x(t, x) / I_x(t, x) \sim 8.5\pm1.0\ \Omega$.

The transmission line was optimized for propagating THz frequencies and designed so that $V_x(t, x)$ and $I_x(t, x)$ are in phase at all points in space and time (i.e. Z_0 is purely real). This was done using a combination of finite element simulations and high frequency circuit simulations. Figure S3b-c plots a simulation of the confined electric field lines of $V_x(t, x)$ at a fixed position in space and time for our transmission line design (cross-sectional view).

Note that as signals propagate in the transmission line they experience some dispersion. We characterize the signal dispersion for our transmission line geometry in section S3.2.

Signal detection. Our measurement directly probes $V_x(t, x)$ at the position $x = x_s$ using a photoconductive switch. x_s is approximately 185 µm relative to the graphene flake in our circuit design. The switch can be modeled as a light-controlled resistor $R_s(t - t') = 1/G_s(t - t')$, operated at time t', that bridges the main signal line to a sampling line. As the signal passes by the switch, $V_x(t, x_s)$ biases the switch. Figure S3c shows the electric field line distribution in the transmission line at the position of the switch, where the field biasing can be seen as a vector field pointing from the signal line towards the sampling line. Without laser illumination, R_s is highly resistive and has little influence on the signal as it passes by. Upon laser illumination, R_s becomes highly conductive and a current $I_s(t, t')$ flows into the contact of the sampling line due to the biasing voltage $V_x(t, x_s)$. By varying t' the temporal profile of $V_x(t, x_s) = Z_0 \cdot I_x(t, x_s)$ can be sampled with ~ 1 ps time resolution.

Signal modelling. In this section, we derive an analytical expression for $V_x(t, x)$ which is directly probed at the photoconductive switch after propagating a distance x_s in the transmission line. For this we take into account the effective capacitance C of our circuitry and the characteristic impedance Z_0 of the transmission line. A simple voltage source model with a DC-voltage bias V and a time-dependent source resistance $R(t)$ (Fig. S3a) is used for modeling the current pulse launched from the graphene. The capacitance C and the impedance Z_0 are considered as a load Z_L in parallel configuration. With the safe assumption that the source resistance R is much larger than the load impedance Z_L we obtain for the time-dependent voltage signal the convolution expression

$$V_x(t, x) \cong Z_0 \cdot I_g(t) * h_{RC}(t) \tag{1}$$

with the impulse response function of the RC-system

$$h_{RC}(t) = \frac{1}{\tau_{RC}} e^{-\frac{t}{\tau_{RC}}} \cdot \theta(t) \tag{2}$$

where $\tau_{RC} \approx Z_0 C$ is the characteristic RC time constant and $\theta(t)$ is the Heaviside step function. The impulse response function $h_{RC}(t)$ describes a first order low-pass characteristic with a cut-off frequency of $f_{RC} = 1 / (2\pi \cdot \tau_{RC})$ and results from the charging and discharging effect of the effective capacitance of the graphene flake. For later discussion we also introduce the transfer function in the frequency domain, which is given by:

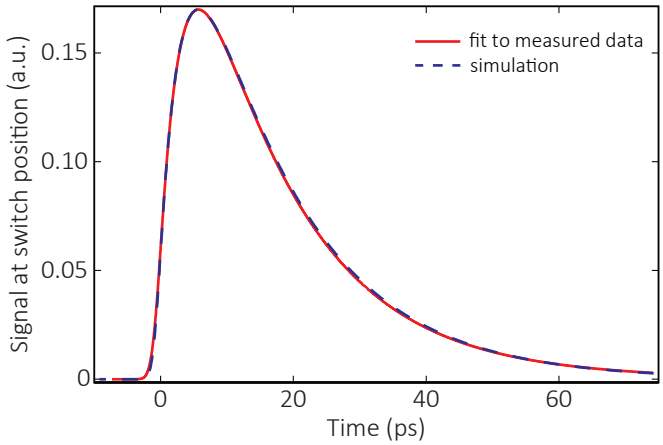

Fig. S4 | Analytical modelling of the effective circuit. Comparison of the analytical model (Eq. 5) used to fit the I_x data in Fig. 3a (main text) with the lumped element circuit simulation. The input parameters for the simulation were σ = 0.8 ps for the pulse duration, the carrier life time in the graphene τ_g = 3.3 ps, and the effective capacitance C = 1.9 pF. The decay time is τ_{RC} = $Z_0 \cdot C$ = 8.5 Ω·1.9 pF = 16 ps. Note that this simulation does not account for propagation-induced signal dispersion in the transmission line, which is characterized in the next section.

$$V_{RC}(\omega) = \frac{1}{1 + i\tau_{RC}\omega} \tag{3}$$

We model the temporal profile of the transient graphene resistance as a convolution of the Gaussian optical pulse profile (of width σ) used to photoexcite the graphene, and an intrinsic photocurrent exponential decay with a characteristic lifetime τ_g. The resulting current can then be expressed as:

$$I_g(t) = \left[\frac{1}{\sqrt{2\pi}\sigma} e^{-\frac{t^2}{2\sigma^2}}\right] * \left[\frac{Q_g}{\tau_g} e^{-\frac{t}{\tau_g}} \cdot \theta(t)\right] \tag{4}$$

where Q_g is the total charge in the generated pulse. Using Eq. 4 as an ansatz for the transfer function defined by Eq. 1 and the impulse response function in Eq. 2, we obtained an expression for the time-dependent voltage:

$$V_0(t,x) \cong \frac{Z_0 Q_g}{2(\tau_{RC} - \tau_g)} \left\{ e^{-\frac{t}{\tau_{RC}} + \frac{\sigma^2}{2\tau_{RC}^2}} \cdot \mathrm{erfc}\left(\frac{1}{\sqrt{2}}\left(\frac{\sigma}{\tau_{RC}} - \frac{t}{\sigma}\right)\right) - e^{-\frac{t}{\tau_g} + \frac{\sigma^2}{2\tau_g^2}} \cdot \mathrm{erfc}\left(\frac{1}{\sqrt{2}}\left(\frac{\sigma}{\tau_g} - \frac{t}{\sigma}\right)\right) \right\} \tag{5}$$

Here erfc(x) is the complementary error function erfc(x) = 1-erf(x). This equation was used to fit the data in Fig. 3a (main text). For the given experiment we assume that $\tau_{RC} \gg \tau_g$.

We checked the analytical model shown in Eq. 5 by using lumped element circuit simulations. We simulated the circuit diagram shown in Fig. S3a and recorded the current profile at the switch position as a function of time. The results are shown in Fig. S4 in comparison to the analytical model. The result shows that a very short pulse is generated in the graphene that subsequently is integrated and discharged by the effective capacitance of the circuitry.

S3.2: Photoconductive switch response, signal dispersion and signal reconstruction

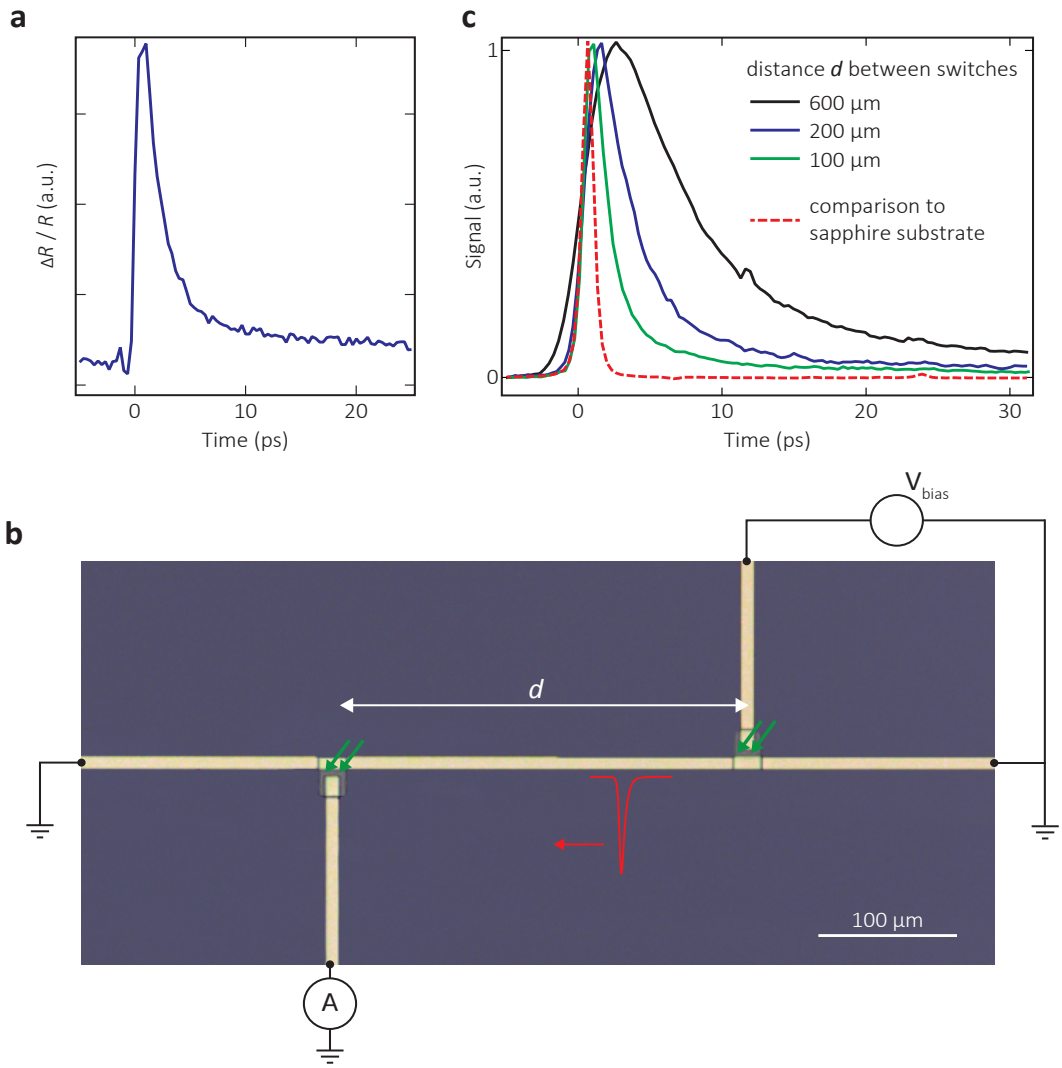

Fig. S5 | Characterization of the photoconductive switch response time and propagation-induced signal dispersion in the transmission line. a, Time-resolved reflectivity measurement of an evaporated silicon film used to construct photoconductive switches. The data indicates a carrier recombination time of ~ 1 ps. **b,** Microscope image of a typical calibration circuit consisting of two photoconductive switches connected by a transmission line. When the biased switch (right) was illuminated with a ~ 500 fs laser pulse, a current pulse was launched into the main transmission line. After propagating a distance *d* down the transmission line, the signal was sampled by a second switch (left). **c,** Sampled current signal at the left photoconductive switch in b, normalized to the peak amplitude. Three calibration circuits built on silicon wafers with d = 100 µm, d = 300 µm, and d = 600 µm shown in b were measured to characterize the propagation-induced signal dispersion in the transmission line. Dashed green line is from a calibration circuit built on a sapphire substrate, where dispersion is negligible, to demonstrate the raw photoconductive switch response time.

In this section we characterize the photoconductive switch response time, propagation-induced signal dispersion in the transmission line, and discuss the procedure used to reconstruct the current signals I_g in the main text.

Photoconductive switch response. We tested the responsiveness of our photoconductive switch design in two ways. (1) Time-resolved optical reflectivity measurements of the evaporated silicon we used to make photoconductive switches and (2) ultrafast current measurements in a calibration circuit comprised of two photoconductive switches.

Reflectivity measurements. We optically characterized the carrier lifetime in our silicon films used to make photoconductive switches by performing time-resolved reflectivity measurements. The result in Fig. S5a shows a carrier recombination time of $\sim$ 1 ps.

Calibration circuit measurement. While the optical measurement shows the carrier lifetime of a clean evaporated silicon film, multiple steps of photolithography are needed to construct photoconductive switches, which change the evaporated silicon properties. To account for this, we directly characterized the typical photoconductive switch response time by performing ultrafast current measurements in a calibration circuit. The circuit used was similar to that shown in Fig. S5b, but built on a sapphire substrate using a coplanar waveguide geometry. We have found that signals exhibit negligible propagation-induced dispersion when built on sapphire substrates, and are therefore well suited to characterizing the raw photoconductive switch response time.

In this measurement, the right switch (Fig. S5b) was biased with a DC voltage and used to launch an ultrafast current pulse into the main transmission line, which was probed by the left switch. By varying the time delay t - t' between the two laser pulses that triggered the switches, the temporal profile of the transient current pulse was obtained. The size of the illuminated area on the switch (< 5 μm) was small compared to the spatial distribution of the transient pulse and is therefore assumed to be a point-like detector. The result for a sapphire device with the two switches separated by 600 μm is shown in Fig. S5c (dashed red line). The signal is symmetric and has a Gaussian width of $\sigma \approx 425$ fs. This signal can be understood as a crosscorrelation of the response functions of the generation switch (GS) and detector switch (DS).

Assuming Gaussian-like identical switch responses for the generator and detector, the autocorrelation stretches the pulse by a factor of $\sqrt{2}$ and we derive that the response time of a single switch is $\sigma \approx 300$ fs.

Propagation-induced signal dispersion in the transmission line. The devices used to measure ultra-fast light-induced anomalous Hall currents in graphene were built on a doped Si/SiO_2 substrate so that the substrate could simultaneously be used as a global backgate to adjust the graphene Fermi level. While ultrafast signals can propagate in microstrip transmission lines built on these substrates, they experience some propagation-induced dispersion. We characterized the propagation-induced signal dispersion in this transmission line geometry by measuring several calibration circuits built on silicon substrates with different distances between the switches. The results are shown in Fig. S5b. As the distance *d* between the switches was increased, the measured signal broadened, demonstrating that propagation-induced dispersion occurs for circuits built on Si/SiO_2.

Signal Reconstruction. To reconstruct the anomalous Hall current signal I_{g} in the graphene, we first corrected the measured Hall signal I_x (Fig. 2, main text) for propagation-induced signal dispersion to recover the undispersed Hall signal I_x', then accounted for the RC low-pass effect caused by the capacitance of the graphene flake to obtain I_{g}. To recover I_x', we first needed to determine the effective transfer function $DISP$ describing the propagation-induced signal dispersion, so that it could be deconvolved from I_x.

I_x can be described as the convolution of I_x', $DISP$, and DS. Note that the detection with a photoconductive switch is described by the crosscorrelation of the signal passing by the switch and DS. For a better overview in this section we quote both, dispersion and detection, as a convolution, since it does not change the argumentation. Because DS was fast compared to I_x, we assumed that DS could be treated as a delta function so that I_x is given by:

$$I_x \approx I_x' * DISP \tag{6}$$

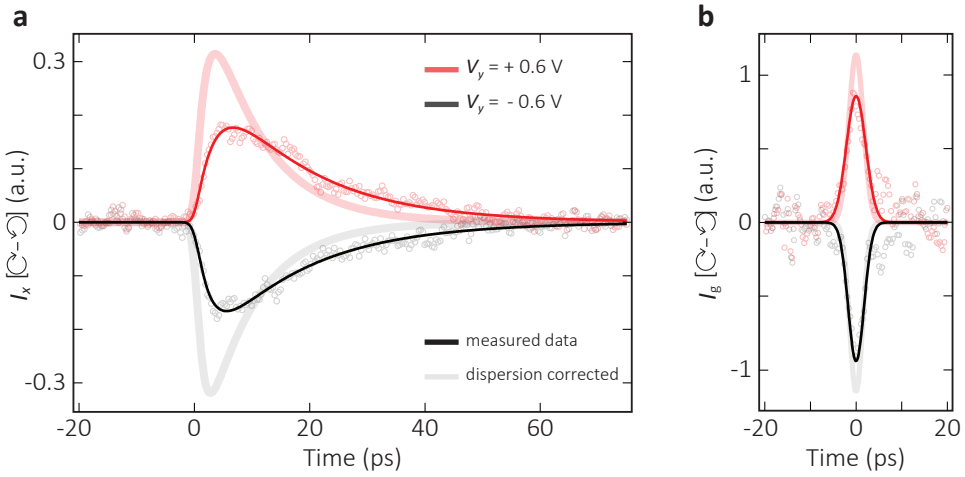

Fig. S6 | **Signal reconstruction. a**, Time-resolved helicity-dependent anomalous Hall currents I_x[↻ - ↺] measured at the photoconductive switch for a positive (red, solid) and negative (black, solid) transverse source-drain voltage V_y. The wide light lines show dispersion corrected data. The graphene Fermi level was gated to the Dirac point (E_F = 0). **b**, Reconstructed anomalous Hall current signals I_g from the raw measured data (solid) and the dispersion corrected data (light).

We estimated $DISP$ by performing measurements on a calibration circuit built on a silicon substrate with the switches 200 µm apart (Fig. S5b, blue curve), where we expect the propagation induced signal dispersion to be approximately equal to that in the graphene device. The measured signal comprises of three elements: The response function of the generation switch (GS), the dispersion induced by the transmission line ($DISP$), and the response function of the detection switch (DS). The signal is thus the convolution $GS * DISP * DS$. Since GS and DS are fast compared to the measured signal, they can be approximated as delta functions, and the convolution becomes $GS * DISP * DS \approx DISP$. Thus, by deconvolving I_x with the blue curve in Fig. S5b, we obtained I_x' (Fig. S6a). The result is that the Hall signal becomes steeper and decays faster.

As discussed earlier, the Hall current I_g in the graphene was integrated by the flake capacitance and then discharged into the transmission line. Thus, we deconvolved the dispersion corrected I_x' data in Fig. S6a with the transfer function for a first-order low-pass filter, which we use to model the current generation (see Eq. 3). We determined τ_{RC} by fitting the exponential decay of I_x'. Figure S6b (light lines) shows the reconstructed current signals accounting for dispersion, which show a time duration of ~ 3 ps (FWHM). The peak amplitude of the Hall signal increases by a factor of ~ 6.0 when comparing the reconstructed signal with the originally measured trace. When dispersion is not accounted for in this analysis, the reconstructed signals have a time duration of ~ 4.5 ps (FWHM).

The reconstructed timescales should be treated as an upper bound on the timescale that anomalous Hall currents persist locally in the graphene. Additional temporal broadening is also expected due to arrival time differences of current signals generated in different parts of the graphene, however we do not expect this to significantly affect the peak amplitude of the reconstructed signal.

S3.3: Estimation of the non-equilibrium anomalous Hall conductance

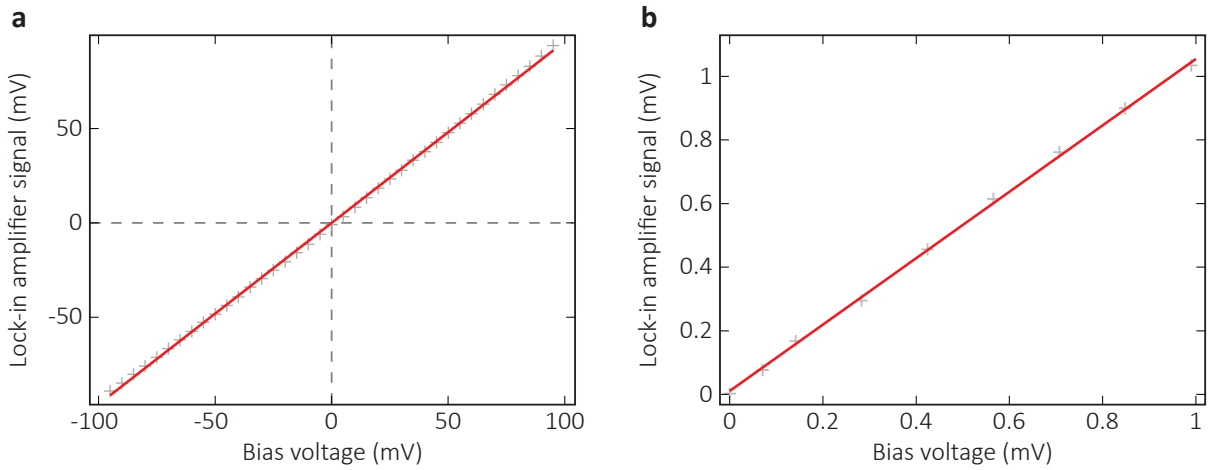

Fig. S7 | **Circuitry calibration.** Measured lock-in amplifier signal of a DC-voltage biased switch triggered with an intensity chopped laser beam. **a**, Calibration for bias voltages in the 100 mV range. **b**, Calibration for bias voltages in the 1 mV range.

The current signal $I_x(x, t)$ propagating in the transmission line carries a voltage $V_x(x, t)$, where the two are related via the transmission line impedance $Z_0 = V_x(t, x) / I_x(t, x) \sim 8.5 \pm 1.0\ \Omega$. At the switch position, we measure a signal using a lock-in amplifier (LIA) that is directly proportional to $V_x(t, x_s)$. To quantitatively determine $V_x(t, x_s)$, we needed to calibrate the LIA reading to a known voltage bias.

To do this, we biased the switch in the graphene device used in the main text with a known DC-voltage and detected the LIA signal upon laser illumination. The graphs in Fig. S7 show the measured LIA signal for a given voltage biasing the switch. A calibration factor lock-in signal / bias voltage of $c_1 = 0.96$ and $c_2 = 1.05$ were determined for 100 mV and 1 mV measurement ranges, respectively. The LIA signals in the Hall current experiment were hundreds of µV, thus we used a calibration factor of $c_2 = 1.05 \pm 0.10$ for the analysis. Because the switch is a point-like and fast detector compared to the spatial and temporal profile of the signal that we detected in the experiment, calibration with a DC voltage bias is a good approximation.

In the general case, the transverse current is given by $I_x = G_{xx}V_x + G_{xy}V_y$. On ultrafast timescales, Hall currents generated in the graphene see the low input impedance Z_0 of the transmission line and leave the sample. Thus, in contrast to DC Hall effect measurements,

there is no V_x Hall voltage accumulation in the graphene and the transverse current is described by $I_x = G_{xy}V_y$. The peak non-equilibrium anomalous Hall conductance is thus given by $G_{xy} = \hat{I}_g[\circlearrowright - \circlearrowleft] / 2V_y$, where $\hat{I}_g$ is the peak of the reconstructed signal in Fig. 3b (main text). The slope of the fitted line in Fig. 4a (main text) gives a value of $V_{LIA} / V_y \approx 105 \times 10^{-6}$. The reconstruction of $\hat{I}_g$ increases this ratio by a factor of ~ 6.0, which yields a peak Hall conductance:

$$G_{xy} = \frac{\hat{I}_g[\circlearrowright - \circlearrowleft]}{2V_y} = \frac{6.0}{c_2 Z_0}\frac{V_{LIA}}{V_y} \approx 1.8 \pm 0.4 \frac{e^2}{h}.$$

The error of the peak Hall conductance arises from small nonlinearities of the switch response (see Fig. S7), the uncertainty in determining the transmission line impedance Z_0, which was obtained from circuit simulations, and the statistical error shown in Fig. 5 (main text).

S4. Photocurrent background at zero source-drain voltage

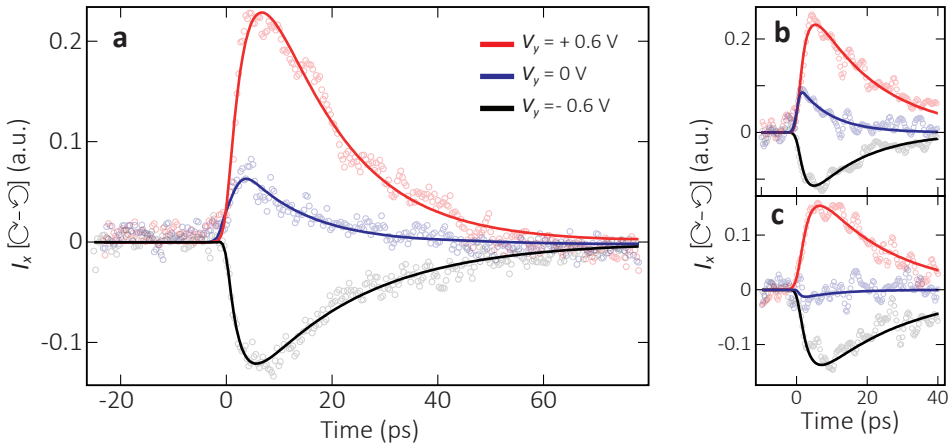

Fig. S8 | Raw Hall current data including a zero source-drain voltage background signal. a, I_x[↻ - ↺] data from Fig. 3a (main text) including the zero source-drain voltage background signal. **b**, and **c**, I_x[↻ - ↺] taken after two different thermal cycles.

A small helicity-dependent photocurrent signal was sometimes observed with no source-drain voltage applied. This signal was recorded during every measurement run and subtracted as a background. We note that after background subtraction, the signals for positive and negative V_y were always symmetric. This background signal likely results from an effective extra bias voltage caused by band bending fields at the contacts.

Figure S8a shows the I_x[↻ - ↺] data presented in Fig. 3 (main text) including the background signal at V_y = 0. This signal exhibited no measurable dependence on the angle of incidence of the light, which rules out the circular photon drag effect[36]. It could be a shift current[37] or a circular photogalvanic current[36] generated at the edge of the graphene flake. While this is an exciting prospect, we believe the signal is more likely due to inhomogeneous band-bending fields at the probing contact. The inhomogeneity can arise as a result of the inhomogeneous doping (responsible for electron-hole puddles) that occurs in graphene[38]. We find that thermal cycling can have a large effect on the relative amplitude of this photocurrent (Fig. S8b-c), in some cases reducing it almost to zero. Based on our observation that the Dirac voltage changes slightly after thermal cycling, we believe that the electron-hole puddle distribution may also be varying. This would in turn affect the inhomogeneity of the band-bending fields. This is an indication that inhomogeneous band-bending fields at the probing contact are the most likely source of this photocurrent.

S5. Results using a different device geometry

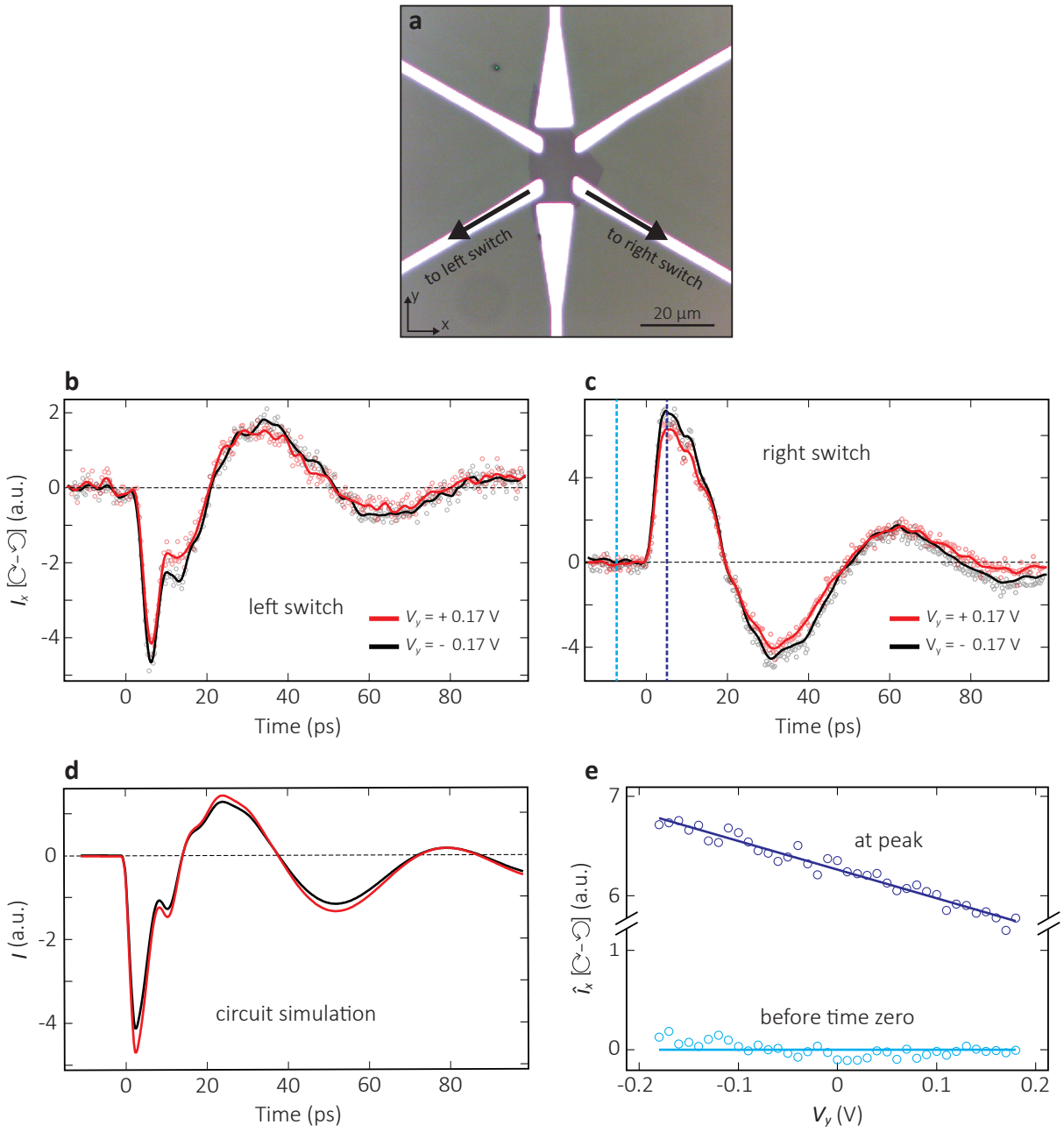

Fig. S9 | **Results from a second device. a**, Optical microscopy image of a graphene device with a different transmission line and contact geometry. Helicity dependent currents I_x[↻ - ↺] measured at the left switch **b**, and right switch **c**, for positive (red) and negative (black) source-drain voltage V_y. **d**, Circuit simulation for the device geometry shown in (a). The simulation takes into account the flake capacitance and the transmission line geometry. The circuit is triggered by a picosecond unipolar pulse with varying amplitude. **e**, Helicity dependent currents $\hat{I}_x$[↻ - ↺] measured as a function of source-drain voltage. The signal is measured before time zero (light blue) and at the peak of the signal (dark blue). The graphene Fermi level was gated to the Dirac point (E_F = 0).

Figure S9 shows the results from a device with a different transmission line and contact geometry from that studied in the main text. This device geometry has certain disadvantages, but we have used it to observe that anomalous Hall signals are generated with opposite polarity at opposite sides of the sample, as expected for any Hall effect.

An optical microscopy image of the device is shown in Fig. S9a. The two large electrodes were used to apply a source-drain voltage V_y. Two of the side transmission lines contacting the flake were equipped with photoconductive switches. Helicity-dependent currents $I_x[\circlearrowright - \circlearrowleft]$ were measured at the right and left photoconductive switches for positive (red) and negative (black) source-drain voltage V_y (Fig. S9b-c).

The first feature of note in these data sets is that there is a larger signal generated at $V_y = 0$ compared to the device studied in the main text (see Fig. S8 for comparison). This signal is not explicitly plotted in Fig. S9b-c, but it resides in between the signals generated with positive and negative V_y. This larger $V_y = 0$ signal is probably due to the asymmetric contact design for this device. For a given probing contact, the band-bending fields in the lower region of the contact can be expected to be modified by the close proximity of the lower source-drain contact. This asymmetry provides a larger effective built-in V_y in the vicinity of the probing contacts compared to the symmetric device design studied in the main text. The gap between the probing contacts and the lower source-drain contact is also smaller than the wavelength of the light used to optically excite the device. Thus, diffraction is expected to reduce the illumination of the graphene in this region. This acts as an additional asymmetry that could contribute to the signal at $V_y = 0$.

The second feature of note is that the signals exhibit large oscillations. These are due to signal reflections at the end of the transmission line, which were $\sim$ 6x shorter compared to those used in the device studied in the main text. The ringing behavior is well modeled by a circuit simulation (see Fig. S9d), similar to the simulation discussed in section S3, which takes into account the geometry of this transmission line design. Nevertheless, using this device we were able to observe the emergence of anomalous Hall currents in graphene (Fig. S9e). We also verified that signals of opposite polarity are generated at opposite sides of the sample, as can be seen by comparing Fig. S9b and S9c. Anomalous Hall current signals were also observed on 3 other devices that explored different device geometries.

S6. Floquet band structure calculations

The system is modeled by a tight-binding Hamiltonian of the form

$$\hat{\mathrm{H}}_{\mathrm{TB}} = t\sum_{\mathrm{j}=1}^{3}\cos\left(\boldsymbol{k}\cdot\boldsymbol{d}_j\right)\hat{\sigma}_x + \sin\left(\boldsymbol{k}\cdot\boldsymbol{d}_j\right)\hat{\sigma}_y \qquad (6)$$

where t denotes the tunneling energy, $\hat{\sigma}_{x,y}$ are the standard Pauli matrices in the basis of Bloch functions residing on the two triangular sub-lattices forming the honeycomb lattice, $\hbar\boldsymbol{k} = \{p_x, p_y\}$ is quasi-momentum and $\boldsymbol{d}_1 = a\{1/2\,, \sqrt{3}/2\}, \boldsymbol{d}_2 = a\{1/2\,, -\sqrt{3}/2\}, \boldsymbol{d}_3 = a\{-1,0\}$ are the vectors connecting nearest-neighbour carbon atoms with spacing $a = 1.42$ Å. We set $t \approx 3.09$ eV such that the Fermi velocity $v_F = 3ta/2\hbar = 10^6 m/s$ [*]. The Dirac points, where the two bands of this Hamiltonian become degenerate, appear at momenta $\boldsymbol{p}_{K,K'} = \{\frac{2\pi}{3a}, \pm\frac{2\pi}{3\sqrt{3}a}\}\hbar$.

In addition, the Hamiltonian in the vicinity of the Dirac points is compared to the approximate Dirac Hamiltonian $\widehat{H}_D = v_F(\tilde{p}_x\hat{\sigma}_x + \tilde{p}_y\hat{\sigma}_y)$ with $\widetilde{\boldsymbol{p}} = \boldsymbol{p} - \boldsymbol{p}_K$. Within the range of energies explored in Fig. 5 (±0.2eV, main text) the static eigenenergies of the two Hamiltonians differ by less than 2 meV.

The electric field of the incident circularly polarized light is then included in the Hamiltonian by working in an accelerated reference frame. That is, we substitute $p_x \to p_{x0} + \frac{eE_R}{\omega}\sin(\omega\tau)$ and $p_y \to p_{y0} + \frac{eE_R}{\omega}\cos(\omega\tau)$ where τ denotes time, e is the electron charge, ω the angular frequency of the light field and $E_R \approx 0.64E_0$ is its peak amplitude, taking into account an effective reduction owing to reflections from the substrate. For this, no shielding from the Graphene flake itself is assumed, whilst the substrate is modeled as stack consisting of a 285 nm SiO_2 layer and a semi-infinite slab of highly doped p-type silicon, with refractive indices at 6.5 μm wavelength of 1.2 and 3.08 + 0.152 i respectively[39].

[*] The next-nearest neighbor tunneling term is left out as it appears as a prefactor to an identity matrix and therefore does not affect the energy difference between the two eigenstates and does not contribute any new terms to the Floquet Hamiltonian.

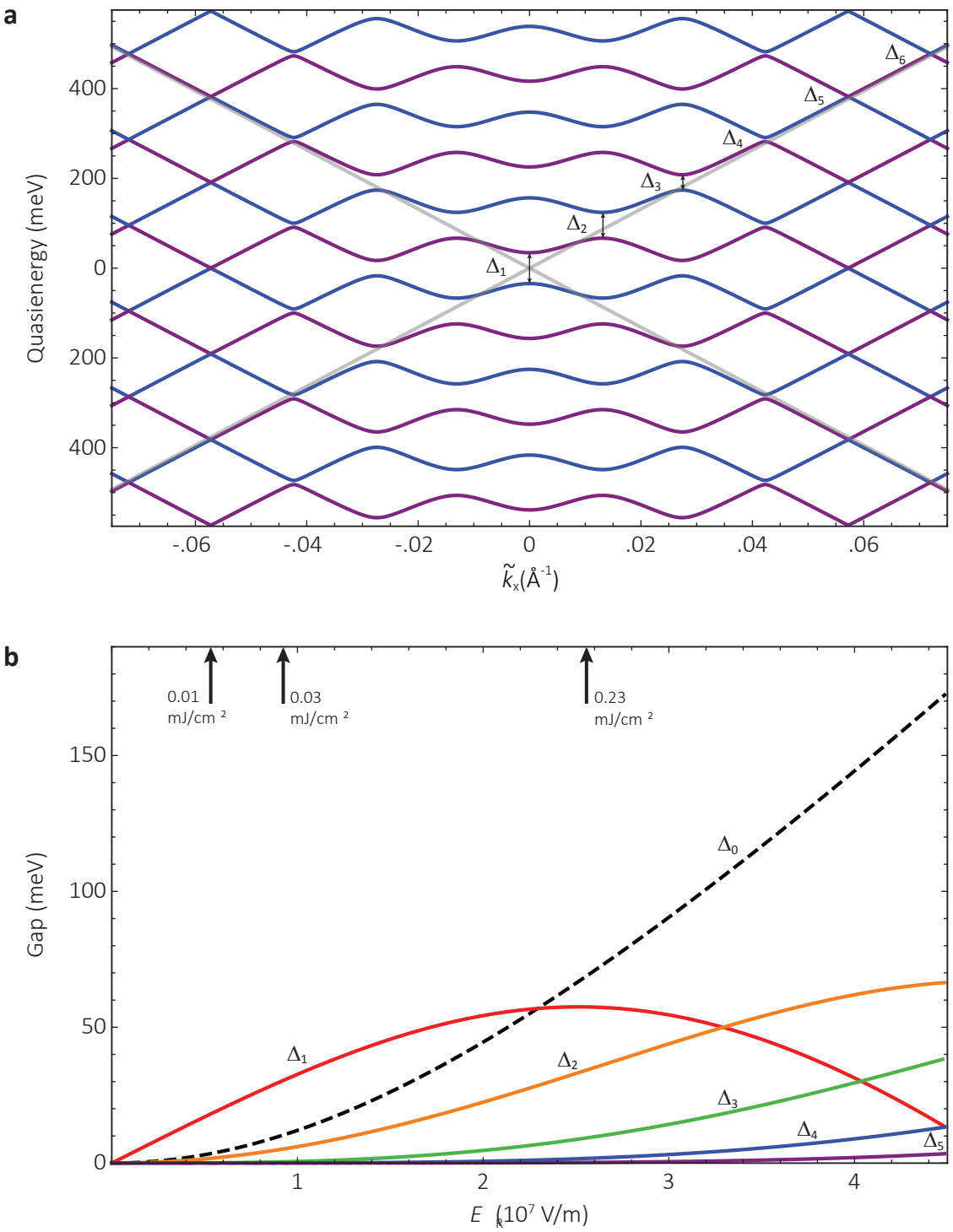

Fig. S10 | Floquet band structure calculations. a, Cut through the Floquet band structure near the Dirac point for the maximum fluence used in the main text. The effective field strength, taking into account reflections from the substrate, is $E_R \approx 2.6 \times 10^7$ V/m. The equilibrium bands are shown in grey, whilst the two Floquet bands are shown in blue and purple, along with their replicas at $\pm n\hbar\omega$. The light-induced gaps are marked with arrows. **b,** Gap size as a function of effective field amplitude. The amplitudes corresponding to the fluences used in the main text are marked with arrows. The gap at the Dirac point is shown as a black, dashed line, whilst the 1st, 2nd, 3rd, 4th and 5th resonant gaps are red, orange, green, blue and purple, respectively.

In order to compute the Floquet band structure, which describes the behavior of periodically driven Hamiltonians on timescales longer than one driving period[8], we determine the unitary evolution operator for one driving period $\mathrm{T} = 2\pi/\omega$. The operator is computed numerically by discretizing the evolution into N steps in real time via

$$\widehat{U}[T,0] = \prod_{j=0}^{N-1} \widehat{U}[(j+1)T/N, jT/N] \approx \prod_{j=0}^{N-1} \mathrm{e}^{-i\widehat{H}jT/N\hbar}$$

We find that for $N \approx 100$ our results deviate from the asymptotic limit by less than 10^{-4} eV. The Floquet spectrum can then directly be extracted by multiplying $\frac{i\hbar}{T}$ with the logarithm of the eigenvalues of $\widehat{U}[T,0]$ at each $\{p_{x0}, p_{y0}\}$. Owing to the invariance of $\widehat{U}$ upon adding or removing energy offsets of $\hbar\omega$ to the Hamiltonian, the Floquet spectrum is periodic in (quasi)energy. Note that whilst the choice of starting phase for the periodic driving (encoded in the time dependence of $\boldsymbol{p}$) does change $\widehat{U}$ and its eigenstates, the spectrum remains invariant.

Figure S10a shows the Floquet spectrum for the same parameters as the third panel in Fig. 5c of the main text, but with an extended range of momenta and energies and with the quasienergy-periodicity explicitly shown. In the main text, only the Floquet bands closest to the static energy were shown, which is where the non-equilibrium electron population is mostly expected[4,27,30].

In addition to the gap at the Dirac point ($\Delta_0 \approx 69$ meV) and the resonant gaps at $\pm\hbar\omega/2$ ($\Delta_1 \approx 56$ meV), gaps also appear at higher-order resonances. The second-order gap still has a significant size of $\Delta_2 \approx 34$ meV, whilst the third-order gap is only 9meV large and further gaps are less than 2 meV. This Floquet spectrum was computed using the full tight-binding Hamiltonian $\widehat{H}_{\mathrm{TB}}$, but for these parameters the results using $\widehat{H}_{\mathrm{D}}$ differ by less than 3 meV in the range plotted here.

Note that for such strong driving, the Floquet bands are shifted somewhat with respect to the equilibrium band, and hence the positions of the gaps are shifted to smaller momenta than in the weak-driving limit. This effect, related to the Bloch-Siegert shift, originates from the low-frequency limit of the Floquet Hamiltonian, where the Floquet bands are given by the average *energy* of the equilibrium band that electrons experience during one cycle[40] (unlike in the high-frequency limit, where the average *Hamiltonian* is experienced). This

average energy is higher (lower) than the static energy on the upper (lower) branch of the Dirac cone.

Figure S10b shows how the size of the gaps scales with the effective electric field amplitude E_{R}. The gap at the Dirac point (black, dashed) initially shows a quadratic dependence on the driving field and then closely follows the exact result obtained for the Dirac Hamiltonian[4] of $\Delta_0 = \sqrt{4(v_F e E_R/\omega)^2 + (\hbar\omega)^2} - \hbar\omega$. For the resonant gaps, we find that the scaling is initially linear for the first-order gap, quadratic for the second-order gap, cubic for the third-order gap etc. However, the gaps then saturate at values around 60 meV and subsequently reduce again. The plotted gaps take into account the aforementioned momentum-shift of the gaps by smoothly following the local minima in the band splitting.

A strong driving field is also expected to lead to a phenomenon known as *dynamical localization*[41], i.e. a reduction of tunnelling in the effective Hamiltonian leading to a flattening of the bands. In the high-frequency limit, this reduction is given by a factor $\mathcal{J}_0(eaE_{\mathrm{R}}/\hbar\omega)$, where $\mathcal{J}_0$ denotes the zeroth-order Bessel function of the first kind. Whilst our calculations do capture this effect when using $\widehat{H}_{\mathrm{TB}}$ (it is absent for $\widehat{H}_{\mathrm{D}}$), we find that it is negligibly small, as expected from the fact that for our parameters this reduction amounts to less than 10^{-4}.

Supplementary references

34. Kozich, V., Moguilevski, A., Heyne, K. High energy femtosecond OPA pumped by 1030nm Yb:KGW laser. *Opt. Commun.* **285**, 4515-4518 (2012).
35. Satirachat, S., Boonrod, P., Kerdsang, W., Haisirikul, N., Suchat, S. Polarization State Control by using Rotating Quarter Wave Plate for the Measurement by Light. *Proc. Eng.* **8,** 243-247 (2011).
36. Glazov, M., Ganichev, S.D. High frequency electric field induced nonlinear effects in graphene. *Phys. Rep.* **535**, 101-138 (2014).
37. Morimoto, T., Nagaosa, N., Topological nature of nonlinear optical effects in solids. *Sci. Adv.* **2**, e150152 (2016).
38. Castro Neto, A. H., Guinea, F., Peres, N. M. R., Novoselov, K. S., Geim, A. K. The electronic properties of graphene. *Rev. Mod. Phys.* **81**, 109-162 (2009).
39. Basu, S., Lee, B. J., Zhang, Z. M. Infrared Radiative Properties of Heavily Doped Silicon at Room Temperature. *J. Heat Transfer* **132**, 023301 (2009).
40. Rodriguez-Vega, M., Lentz, M., Seradjeh, B. Floquet perturbation theory: formalism and application to low-frequency limit. *New J. Phys.* **20**, 093022 (2018).
41. Grifoni, M., Hänggi, P. Driven quantum tunneling. *Physics Reports* **304**, 229-354 (1998).